Naval Research Laboratory

Washington, DC 20375-5320

NRL/MR/6790--12-9432

Non-Force-Free Magnetic Flux Ropes with Minimum Complexity in an Ambient Medium: A Parameter Study

JAMES CHEN

Beam Physics Branch
Plasma Physics Division

October 16, 2012

REPORT DOCUMENTATION PAGE

Form Approved
OMB No. 0704-0188

1. REPORT DATE *(DD-MM-YYYY)*	**2. REPORT TYPE**	**3. DATES COVERED** *(From - To)*
16-10-2012	Interim	May 2012 – July 2012

4. TITLE AND SUBTITLE

Non-Force-Free Magnetic Flux Ropes with Minimum Complexity in an Ambient Medium: A Parameter Study

5a. CONTRACT NUMBER

5b. GRANT NUMBER

5c. PROGRAM ELEMENT NUMBER
67-9871-02

6. AUTHOR(S)

James Chen

5d. PROJECT NUMBER

5e. TASK NUMBER

5f. WORK UNIT NUMBER

7. PERFORMING ORGANIZATION NAME(S) AND ADDRESS(ES)

Naval Research Laboratory
4555 Overlook Avenue, SW
Washington, DC 20375-5320

8. PERFORMING ORGANIZATION REPORT NUMBER

NRL/MR/6790--12-9432

9. SPONSORING / MONITORING AGENCY NAME(S) AND ADDRESS(ES)

Office of Naval Research
875 North Randolph Street, Suite 1425
Arlington, VA 22203-1995

10. SPONSOR / MONITOR'S ACRONYM(S)

ONR

11. SPONSOR / MONITOR'S REPORT NUMBER(S)

12. DISTRIBUTION / AVAILABILITY STATEMENT

Approved for public release; distribution is unlimited.

13. SUPPLEMENTARY NOTES

14. ABSTRACT

The structure and properties of non-force-free (NFF) equilibrium magnetic flux ropes in an ambient medium of specified pressure p_a have been studied in detail. A flux rope is a self-organized magnetized plasma structure consisting of a localized channel of electric current and the magnetic field arising from this current. An analytic method has been developed to obtain one-dimensional equilibrium solutions satisfying $\mathrm{J}\times\mathrm{B}-\nabla p=0$ subject to the requirements that (1) all physical quantities be nonsingular and continuous, (2) pressure $p(r)$ be physically admissible—real and nonnegative, and (3) the magnetic field profile have "minimum complexity." The basic theory and a limited parameter study have been published elsewhere. In the present report, a more comprehensive study extending the previous work to a new parameter regime is provided. The solutions are characterized by two parameters, $B_t^* \equiv \bar{B}_t/(8\pi p_a)^{1/2}$ and $B_p^* \equiv B_{pa}/(8\pi p_a)^{1/2}$, where $\bar{B}_t$ is the toroidal (axial) field averaged over the cross-sectional radius a and B_{pa} is the poloidal (azimuthal) field at the edge of the current channel ($r = a$). The physical constraints on pressure—nonnegative and real pressure—define equilibrium boundaries in the B_t^*–B_p^* space beyond which no physical solutions exist.

15. SUBJECT TERMS

Solar plasma physics
Interplanetary plasma physics
Magnetohydrodynamics (MHD)
Magnetic flux ropes

16. SECURITY CLASSIFICATION OF:			**17. LIMITATION OF ABSTRACT**	**18. NUMBER OF PAGES**	**19a. NAME OF RESPONSIBLE PERSON**
a. REPORT	**b. ABSTRACT**	**c. THIS PAGE**			James Chen
Unclassified Unlimited	Unclassified Unlimited	Unclassified Unlimited	Unclassified Unlimited	36	**19b. TELEPHONE NUMBER** *(include area code)* (202) 767-3134

Standard Form 298 (Rev. 8-98)
Prescribed by ANSI Std. Z39.18

Non-Force-Free Magnetic Flux Ropes With Minimum Complexity in an Ambient Medium: A Parameter Study

James Chen

Plasma Physics Division, Naval Research Laboratory, Washington, DC

ABSTRACT

The structure and properties of non-force-free (NFF) equilibrium magnetic flux ropes in an ambient medium of specified pressure p_a have been studied in detail. A flux rope is a self-organized magnetized plasma structure consisting of a localized channel of electric current and the magnetic field arising from this current. An analytic method has been developed to obtain one-dimensional equilibrium solutions satisfying $c^{-1}\mathbf{J} \times \mathbf{B} - \nabla p = 0$ subject to the requirements that (1) all physical quantities be nonsingular and continuous, (2) pressure $p(r)$ be physically admissible—real and nonnegative, and (3) the magnetic field profile have "minimum complexity." The basic theory and a limited parameter study have been published elsewhere. In the present report, a more comprehensive study extending the previous work to a new parameter regime is provided. The solutions are characterized by two parameters, $B_t^* \equiv \bar{B}_t/(8\pi p_a)^{1/2}$ and $B_p^* \equiv B_{pa}/(8\pi p_a)^{1/2}$, where $\bar{B}_t$ is the toroidal (axial) field averaged over the cross-sectional radius a and B_{pa} is the poloidal (azimuthal) field at the edge of the current channel ($r = a$). The physical constraints on pressure—non-negative and real pressure—define equilibrium boundaries in the B_t^*–B_p^* space beyond which no physical solutions exist.

Manuscript approved Septemver 10, 2012

1. Introduction

A study was recently made of the equilibrium structure of non-force-free (NFF) magnetic flux ropes placed in an ambient medium where the pressure gradient force is nonzero (Chen 2012, henceforth referred to as Paper 1). The work is formulated using standard magnetohydrodynamics (MHD) and develops a new physical constraint termed "minimum complexity." Analytic solutions were given satisfying specified physical conditions with a limited parameter study. The present report extends the discussion in Paper 1 and provides a more comprehensive documentation of the solution set as well as an additional family of solutions that has not been previously published. The basic physics, however, remains unchanged.

Magnetic flux ropes are important building blocks of the solar corona and interplanetary medium. A flux rope is a self-organized magnetized plasma structure consisting of an electric current distribution $\mathbf{J}(\mathbf{x})$ and its magnetic field $\mathbf{B}(\mathbf{x})$ embedded in an ambient medium of pressure p_a. The magnetic field enables a flux rope to maintain its structural identity separate from the ambient plasma. In natural plasma environments, flux ropes reside in background plasmas. They are generally curved, with the local geometry characterized by major radius R and minor radius a. For $R/a \gg 1$, the minor radial forces can be approximated by those acting on a straight cylinder (e.g., Shafranov 1966). Although this approximation incurs an error of $\mathcal{O}(a/R)$ and becomes less accurate as R/a approaches unity, the simple configuration can capture the essential structure of flux ropes.

Within the framework of MHD in which the internal structure of an equilibrium flux rope in the absence of gravity is determined by $(1/c)\mathbf{J} \times \mathbf{B} = \nabla p$, where $\mathbf{J} = (c/4\pi)\nabla \times \mathbf{B}$. A particular limiting case, the "force-free" (FF) approximation defined by $c^{-1}\mathbf{J} \times \mathbf{B} = 0$, has been widely studied because of mathematical simplicity. These mathematical FF solutions (e.g., Lundquist 1950), however, make no reference to the ambient pressure and for specific applications, may not satisfy the physical boundary conditions dictated by a magnetic flux rope embedded in a plasma medium of pressure p_a. The method presented in Paper 1 self-consistently solves the basic one-dimensional (1D) MHD equation subject to specified asymptotic ambient pressure p_a. Furthermore, the solutions satisfy requirements that (1) physical quantities be everywhere continuous and nonsingular, (2) pressure $p(r)$ be real and nonnegative (and smoothly converge to the ambient value p_a), and (3) the magnetic field profile have "minimum complexity." No specific radial dependence of $p(r)$ or $\mathbf{B}(r)$ is prescribed. The derivation of the method shows that the solutions can be specified by two dimensionless parameters, $B_t^* \equiv \bar{B}_t/(8\pi p_a)^{1/2}$ and $B_p^* \equiv B_{pa}/(8\pi p_a)^{1/2}$, where $\bar{B}_t$ is the toroidal (locally axial) field averaged over the minor radius and B_{pa} is the poloidal (locally azimuthal) field at the edge of the current channel, $r = a$. The requirement of real and

nonnegative pressure defines equilibrium boundaries beyond which no physical equilibrium solutions exist. Paper 1 also demonstrated that the average internal pressure $\overline{p}$ can be separately specified. Some basic properties of the self-consistent equilibrium were illustrated with one solution for a specified value of $\overline{p}_s = 0.85$. One value of $\overline{p}_s$, however, determines only one sub-family of solutions. In the present report, the treatment is extended to provide a fuller examination of NFF equilibrium solutions in parameter regimes that were not discussed in the earlier report.

The basic formulation is given in Paper 1 and is not repeated here. The present report is not self-contained but is intended to supplement Paper 1. The specific equilibrium solutions given here can be used to infer the qualitative properties of solutions that are not specifically presented. By way of defining symbols and physical quantities, an abbreviated derivation of the relevant equations is given in Section 2 below. Sections 3–5 provide the new material.

2. One-Dimensional Non-Force-Free (NFF) Flux Ropes

The forces acting on a straight cylindrical flux rope are considered in the framework of standard MHD. In equilibrium the applicable equations are

$$\frac{1}{c}\mathbf{J} \times \mathbf{B} - \nabla p = 0, \tag{1}$$

$$\mathbf{J} = \frac{c}{4\pi}\nabla \times \mathbf{B}, \tag{2}$$

$$\nabla \cdot \mathbf{B} = 0. \tag{3}$$

Gravity is neglected. We use a cylindrical coordinate system with the axis of the flux rope aligned with the z (toroidal) direction, as illustrated in Figure 1. The radial coordinate measured from the axis of the cylinder is r, with the electric current $\mathbf{J}$ limited to $r \leq a$. The poloidal (locally azimuthal) angle is denoted by θ. The treatment is 1D, and we impose $\partial/\partial z = \partial/\partial\theta = 0$. Pressure is $p(r)$ with the asymptotic ambient pressure p_a taken to be constant consistent with the neglect of gravity.

The current density has components $J_p(r)$ and $J_t(r)$ in the poloidal and toroidal directions, producing toroidal $B_t(r)$ and poloidal $B_p(r)$ magnetic field components, respectively. Because of the assumed cylindrical symmetry, the magnetic field has the general structure $\mathbf{B}(r) = (0, B_p(r), B_t(r))$ with $\mathbf{J}(r) = (0, J_p(r), J_t(r))$, and the condition $\nabla \cdot \mathbf{B} = 0$ is trivially satisfied. Inside the current channel ($r \leq a$), the magnetic field "lines" are helical. This is schematically illustrated in Figure 1 with one representative helical curve. Outside the current channel ($r > a$), we have $\mathbf{J}(r) = 0$ and $B_p(r) = B_{pa} \cdot (r/a)^{-1}$ and $B_t(r) = 0$ regardless

of the profile of $\mathbf{J}(r)$ for $r \leq a$. Here, $B_{pa} \equiv B_p(r=a)$. By flux rope, we refer to the entire system consisting of the current channel defined by $\mathbf{J}(r) \neq 0$ ($r \leq a$) and the magnetic field including that for $r > a$ attributable to this $\mathbf{J}(r)$ according to Ampere's law. The flux rope is embedded in a plasma medium of density n and temperature T, with pressure $p(r) = p_i(r) + p_e(r) = 2nkT$, where we have assumed $T_i = T_e$. Subscripts i and e refer to ions and electrons, respectively.

In this cylindrical coordinate system, equation (1) takes on the form

$$\frac{dp}{dr} = -\frac{1}{8\pi}\frac{dB^2}{dr} - \frac{1}{4\pi}\frac{B_p^2}{r}, \tag{4}$$

where $B^2 = B_p^2 + B_t^2$ and $\partial/\partial\theta = 0$ and $\partial/\partial z = 0$ have been used. Now define the dimensionless variable $x \equiv r/a$ and form functions $b_p(x)$ and $b_t(x)$ such that

$$B_p(x) = B_{pa} b_p(x), \quad B_t(x) = \overline{B}_t b_t(x). \tag{5}$$

Here, $B_{pa} \equiv B_p(x=1)$ and $\overline{B}_t$ is the toroidal field averaged over the cross-section,

$$\overline{B}_t \equiv 2\pi \int_0^a B_t(r) r dr/\pi a^2 = 2\overline{B}_t \int_0^1 b_t(x) x dx. \tag{6}$$

These definitions lead to the general properties

$$b_p(1) = 1, \quad \overline{b}_t \equiv 2\int_0^1 b_t(x) x dx = 1, \tag{7}$$

and Ampere's law takes on the dimensionless form

$$j_p(x) = -\frac{db_t(x)}{dx}, \quad j_t(x) = \frac{1}{x}\frac{d}{dx} x b_p(x), \tag{8}$$

with the dimensional current densities given by $J_p(x) = (c/4\pi)(\overline{B}_t/a) j_p(x)$, and $J_t(x) = (c/4\pi)(B_{pa}/a) j_t(x)$. Ampere's law leads to $B_{pa} = 2I_t/ca$, where $I_t \equiv 2\pi a^2 \int_0^1 x J_t(x) dx$ is the total toroidal current integrated over the cross-section of the flux rope. This is equivalent to

$$\int_0^1 x j_t(x) dx = 1, \tag{9}$$

which is in turn equivalent to $b_p(1) = 1$. Localization of the current to $x \leq 1$ with no discontinuity at $x = 1$ requires

$$j_p(x \geq 1) = 0, \quad j_t(x \geq 1) = 0. \tag{10}$$

All the solutions of this system can be characterized by the following two dimensionless parameters:

$$B_p^* \equiv \frac{B_{pa}}{(8\pi p_a)^{1/2}}, \quad B_t^* \equiv \frac{\overline{B}_t}{(8\pi p_a)^{1/2}}. \tag{11}$$

2.1. Minimum Complexity

Equation (4) with the physical conditions still admits an infinity of solutions. In order to construct unique solutions, the functional form of $b_t(x)$ and $b_p(x)$ must be constrained. Previously, the FF equation, $\mathbf{J} \times \mathbf{B} = 0$, has been solved using the assumption that $\mathbf{J}(x)$ and $\mathbf{B}(x)$ have exactly the same functional form, satisfying $\mathbf{J}(x) = \alpha \mathbf{B}(x)$ at every point x, where α is a constant (Lundquist 1950). Typically, this mathematical solution is used without reference to specific boundary conditions. The so-called Lundquist solution may be applicable in certain confined laboratory systems with closed magnetic surfaces by assuming that turbulent dissipation would render α constant in space while leaving the total magnetic helicity unchanged (Taylor 1974) or by assuming that the system is in the lowest magnetic energy state (Woltjer 1958). Paper 1 adopted an alternative hypothesis: a flux rope "relax" to a state with "minimum complexity" subject to imposed conditions. The system need not be closed, and no dissipation is required. Physically, this is a conjecture motivated by the expectation that a plasma system evolves to minimize gradients in $\mathbf{B}(\mathbf{x})$ and $p(\mathbf{x})$ everywhere while conforming to some external constraints imposed by the macroscopic system.

Mathematically, minimum complexity solutions are constructed as follows. First, the cross-sectional radius is characterized by one length scale, a. Accordingly, $b_p(x)$ and $b_t(x)$ are expanded in terms of $x = r/a$ and demand that the polynomial representation satisfy the required constraints with the smallest number of terms. This ensures that there are fewest extrema. Thus, we seek solutions of the form

$$b_p(x) = \sum_{m=0}^{M} h_m x^m, \tag{12}$$

and

$$b_t(x) = \sum_{n=0}^{N} d_n x^n, \tag{13}$$

and choose the smallest M and N according to the number of constraints. From equation (8), we obtain

$$j_p(x) = -\sum_{n=0}^{N} n d_n x^{n-1}, \tag{14}$$

and

$$j_t(x) = \sum_{m=0}^{M} (m+1) h_m x^{m-1}. \tag{15}$$

In this formulation, the minimum complexity hypothesis is a macroscopic constraint, not a condition imposed on each point x in space.

3. Alternative Solution 1

The physical constraints listed above uniquely determine the functional forms of $b_t(x)$ and $b_p(x)$ subject to the mathematical condition that the lowest-order powers in x be used. There is, however, a degree of freedom in choosing the specific form of the functional forms. In this section, this freedom is illustrated.

The family of solutions S1 discussed in section 3.1 of Paper 1 uses the lowest three nonzero terms in x^n for $b_t(x)$ and $b_p(x)$. Instead, one may use the lowest three nonzero even powers for $b_t(x)$ and nonzero odd powers for $b_p(x)$. Accordingly, we choose $n = 0, 2, 4$ and $m = 1, 3, 5$. The solution of the equation of equation (4) is then

$$b_t(x) = \begin{cases} 3\,(1 - 2x^2 + x^4), & x \leq 1 \\ \\ 0, & x > 1, \end{cases} \tag{16}$$

and

$$b_p(x) = \begin{cases} 3x(1 - x^2 + x^4/3), & x \leq 1, \\ \\ x^{-1}, & x > 1. \end{cases} \tag{17}$$

We will refer to this solution as Alternative Solution 1, denoted by S1a. Ampere's law yields

$$j_p(x) = 12x(1 - x^2), \tag{18}$$

$$j_t(x) = 6\,(1 - 2x^2 + x^4), \tag{19}$$

inside the current channel ($x \leq 1$). As before, outside the current channel, we have $j_t(x) = 0$ and $J_p(x) = 0$ for all $x > 1$.

The normalized self-consistent pressure is given by

$$\hat{p}(x) = \hat{p}_0 - [B_p^{*2} b_p^2(x) + B_t^{*2} b_t^2(x) - 9B_t^{*2}] - 9B_p^{*2} x^2 \left(1 - x^2 + \frac{5}{9}x^4 - \frac{1}{6}x^6 + \frac{1}{45}x^8\right), \quad x \leq 1, \tag{20}$$

for inside the current channel.

Outside the current channel, the pressure is

$$\hat{p}(x) = \hat{p}_0 - \frac{47}{10}B_p^{*2} + 9B_t^{*2} = 1, \quad x \geq 1, \tag{21}$$

which is manifestly constant. This leads to

$$\hat{p}_0 = 1 + (47/10)B_p^{*2} - 9B_t^{*2}. \tag{22}$$

The volume-averaged internal pressure is given by $\overline{p} \equiv 2\int_0^1 x\hat{p}(x)dx$. For S1a, it is simply

$$\overline{p} = 1 + B_p^{*2} - \left(\frac{9}{5}\right) B_t^{*2}. \tag{23}$$

Thus, the equilibrium solutions for a given value of $\overline{p}$ lie on the curve given by

$$B_p^* = \left(\frac{9}{5}B_t^{*2} - 1 + \overline{p}\right)^{1/2}. \tag{24}$$

By demanding $B_p^* \geq 0$, this equation shows that $\overline{p} \geq 0.8$ for all physically allowed choices of B_p^* and B_t^*. Here recall that for $B_p^* = 0$, the allowed solutions have $0 \leq B_t^* \leq 1/3$.

The allowed equilibrium solutions with non-negative pressure satisfy the condition

$$B_p^* \geq \left(\frac{10}{47}\right)^{1/2} \left(9B_t^{*2} - 1\right)^{1/2}. \tag{25}$$

This boundary is similar to curve A in Figure 2 of Paper 2 as are the other boundary curves in the B_p^*–B_t^* space.

Figure 2 shows a particular solution of this family specified by $B_t^* = 0.5$ and $B_p^* = 0.69189841$. This solution is the counterpart of S1.1 discussed in Paper 1 (Figure 3, Paper 1) in that it lies on the asymptote to the equilibrium (counterpart of line B in Figure 2 of Paper 1) with $B_t^* = 0.5$ and has $\hat{p}(0) = 1$. Comparing this solution with S1.1, it is clear that the field configurations and current distributions are virtually identical. This can also be seen from the value $\xi = 1.7448$ for S1.1a, which is similar to $\xi = 1.7690$ for S1.1, where

$$\xi \equiv (B_t)_{max}/(B_p)_{max}. \tag{26}$$

The most visible difference is that for S1.1a, the peak of $B_t(x)$ is slightly broader and $J_p(x)$ is peaked slightly farther away from the axis than for S1.1. For solution S1.1a, we obtain $\mathcal{D}_p = 6.0637 \times 10^{-2}$. The quantitative similarity between S1.1 and S1.1a is due to the fact that the low-order powers x^3 and x^4 are similar in the range $0 \leq x \leq 1$. Figure 3 shows the Alfvén velocity $V_A(x)$ and plasma $\beta(x)$ for S1.1a, which resemble those of S1.1. For S1.1a, we find $\beta(0) = 0.4444$ and $\overline{\beta} = 1.2071$.

For S2 and S3, similar freedom in choosing the power of x exists. If, however, higher-order terms are introduced, additional extrema in the current channel may occur, violating the minimum complexity condition. Thus, the ability to choose different functional forms for $b_t(x)$ and $b_p(x)$ is limited.

4. Force-Free Limits

In this section, we extend the discussion on the FF limit and low-β limit previously given in section 4 of Paper 1, where the limiting properties of the class of solutions S1 were calculated along a line through the origin with a slope of $B_p^*/B_t^* = (350/159)^{1/2}$ (Figure 2, Paper 1). Specifically, consider $\beta(x)$ and pressure gradient $d\hat{p}(x)/dx$ averaged over the volume of the current channel:

$$\overline{\beta} \equiv 2\int_0^1 x\beta(x)dx, \quad \text{and} \quad \mathcal{D}_p \equiv 2\int_0^1 x\left|\frac{d\hat{p}(x)}{dx}\right|dx. \tag{27}$$

Here, the local plasma is given by $\beta(x) = 8\pi p(x)/B^2(x)$, and

$$\beta(0) = \frac{\hat{p}(0)}{B_t^{*2}b_t^2(0)}, \quad \text{and} \quad \beta(1) = \frac{1}{B_p^{*2}}. \tag{28}$$

Noting that $\beta = (2v_{th}/V_A)^2$, nonuniform $\beta(x)$ suggests that a flux rope is not "monolithic" in its structural robustness as it evolves over time. Here, $v_{th} = (kT/m)^{1/2}$ is the thermal speed.

Shown in Figure 4 are the quantitative properties of $\overline{\beta}$ and $\mathcal{D}_p$ for the two distinct limits $B_p^* \to 0$ and $B_p^* \to \infty$ of the family of solutions S1. Figure 4a shows $\overline{\beta}$ and $\mathcal{D}_p$ as well as $\beta(0)$ and $\beta(1)$, defined by equations 27 and 28, respectively, along a line through the origin with slope $B_p^*/B_t^* = 2/3$, where the values of β (solid and dash-dot) and $\mathcal{D}_p$ (dashed) are shown on the left and right vertical axes, respectively. On this line, all solutions have $\xi = 3.0370$ and identical field profiles. This line intersects the equilibrium boundary (curve A in Figure 2, Paper 1) at $B_p^* = 0.223873$. This value is indicated by the vertical line A in Figure 4a, where the solution yields $\hat{p} = 0$ and therefore $\beta(0) = 0$, while $\overline{\beta} = 8.3916$ (left axis) and $\beta(1) = 19.9524$. This solution has $\mathcal{D}_p = 0.3638$ at A. Beyond this point, no physical solutions exist. The limit $B_p^* \to 0$ leads to $\beta \to \infty$, where the flux rope has $\mathcal{D}_p = 0$, i.e., $d\hat{p}(x)/dx = 0$ for all x. This is the FF limit.

Figure 4b shows the same quantities along a line of slope $B_p^*/B_t^* = 2$. Again, in the limit $B_p^* \to 0$, we obtain $\beta \to \infty$ and $\mathcal{D}_p \to 0$. Flux ropes are nearly FF and have high β in the neighborhood of this limit. According to equation (28), the limit $B_p^* \to \infty$ leads to $\beta(1) = 0$. On the axis of the flux rope, however, β converges to $\beta(0) = 0.8172$ with $\overline{\beta} = 0.2323$ (left axis). The flux rope becomes highly NFF in this limit with $\mathcal{D}_p \to \infty$.

In the solar physics literature, the common adage is that the coronal plasma β is so small ($\beta \to 0$) that the force-free approximation ($c^{-1}\mathbf{J} \times \mathbf{B} = \nabla p = 0$) is valid. The above results and those of Paper 1 contradict this adage. Because this adage implicitly underlies the solar physics literature, it warrants some attention. By remote sensing techniques, the

coronal pressure p_a can be estimated at various heights, but the local coronal magnetic field cannot be measured at this time. Instead, the magnitudes $B = |\mathbf{B}|$ of coronal magnetic fields are estimated from photospheric magnetograms using various simplifications such as the FF approximation. Using the estimated "typical" value B' of the coronal field and the estimated p_a, an effective plasma β is defined by $\beta' \equiv 8\pi p_a/B'^2$. Depending on the value of B' chosen in these estimates, β' may indeed be small. The magnetic field of a plasma structure embedded in a plasma medium, however, cannot be specified a priori. Instead, B must be determined self-consistently based on actual force balance. We have defined a self-consistent effective plasma β as follows:

$$\beta' \equiv \frac{8\pi p_a}{< B(x)^2 >}, \tag{29}$$

where $B(x)$ is the self-consistently calculated magnetic field in force balance with p_a and $< \ldots >$ is the volume average over the current channel. This effective β' is plotted in Figures 4a and 4b as dotted curves. The plots show that β' behaves similarly to the local β and $\overline{\beta}$ along the two lines in the parameter space: $\beta' \to \infty$ in the FF limit as $\mathcal{D}_p \to 0$. The usual adage is no more valid in terms of β' than in terms of the actual β. This is consistent with the conclusion given in Section 4 of Paper 1.

5. Specification of Average Internal Pressure $\overline{p}$

For S3, the parameter space structure depends on the specified value of $\overline{p}_s$. Section 3.3 of Paper 1 describes in detail one particular solution belonging to the sub-family of solutions, S3.0, defined by $\overline{p}_s = 0.85$. In this section, a more comprehensive discussion of this family of solutions is given for several values of $\overline{p}_s$. Figure 5 shows the B_t^*–B_p^* parameter space for S3.0. Several particular solutions are indicated by the numbered dots, "1"–"5." These solutions will be designated S3.01–S3.05, respectively. The boundary curve A is defined by $\hat{p}(0) = 0$ with $\hat{p}(0) < 0$ on the left of A. To the right of curve B, pressure $\hat{p}(x)$ develops a non-zero imaginary part. The short line segment "a" indicates the value of B_p^* beyond which no physical solutions exist, and the open diamond represents the only solution, S3.06, with real and nonzero $\hat{p}(x)$ at this B_p^*, which is $B_p^* = 1.002834$. The line segment "b" is at $B_p^* = 0.3350$ below which all solutions between A and B are physically acceptable. The open diamond (b) is at $B_t^* = 0.360$ and $B_p^* = 0.3350$. Above b, some solutions near A and B are not physical because $\hat{p}_{min}$ becomes negative.

S3.01 has been presented in Paper 1 and will not be discussed here. Figure 6 shows the magnetic field, electric current, and pressure profiles of S3.02, where the constant-α Lundquist solution is shown (dash-dot curves) for comparison. This solution, indicated by

"2" in Figure 5, is slightly to the right of equilibrium boundary A. For this solution, $\hat{p}_{min} \approx 0$ occurs at $x = 0.082$. The average pressure gradient is $\mathcal{D}_p = 0.4075$. Figure 7 shows the Alfvén speed $V_A(x)$ (solid curve, left axis) and plasma β (dashed curve, right axis). Because of the relatively low pressure near the axis, we have $\beta \ll 1$. For this flux rope, $\beta_{min} = 8.3383 \times 10^{-3}$ and V_{Amax} occur at $x = 0.082$, and β exceeds unity at about $x = 0.50$, reaching $\beta \approx 5$ at $x = 1$. Overall, $\overline{\beta} = 2.5560$.

Figures 8–13—solutions labeled "3"–"5" in Figure 5—describe a variety of representative solutions in the physically allowable parameter space, showing the profiles of magnetic field, current, pressure, Aflvén speed, and plasma β. Here, dash-dot curves show the magnetic field components of the constant-α Lundquist solution for comparison. These solutions are chosen to be near the boundary curves A and B.

Above b, as boundary A is approached from the right, $\hat{p}_{min}$ occurs away from the axis so that $\hat{p}_{min} < \hat{p}(0)$. This leads to $\hat{p}_{min}$ becoming negative before $\hat{p}(0)$ becomes zero, i.e., at a point to the right of A. Figures 8 provides an example. This is in contrast to the behavior below b where $\hat{p}_{min}$ occurs at $x = 0$ on the boundary curve A. Above "b," $\hat{p}_{min}$ also becomes negative before $\hat{p}(x)$ becomes complex. Above b, there is a band adjacent to each of A and B where the solutions develop $\hat{p}_{min} < 0$ and become unphysical. As B_p^* is increased between b and a, these bands broaden, and $\hat{p}_{min} < 0$ sets in farther away from A or B until at b where $B_p^* = 0.3350$ only one physical solution exists. Figures 12 and 13 show the properties of a representative solution slightly below a. Note that $\hat{p}(0)$ increases with B_p^*. The solution labeled "a" is not significantly different from S3.05 in magnetic field and pressure profiles and is not shown. The solution at "a" is designated as S3.06, for which $B_p^* = 1.002834$, the numerical values of $\beta_{min} = 7.2004 \times 10^{-8}$ and $(V_A)_{max}/V_{A0} = 2.6435 \times 10^3$ are obtained. This shows that to within numerical accuracy $\beta_{min} \to 0$ and $(V_A)_{max} \to \infty$ for the true upper limit of the physically allowed value of B_p^*. For the S3.0 sub-family of solutions, there exists no FF limit because $\overline{p}_s < 1$, and the limit $B_t^* \to 0$ and $B_p^* \to 0$ is not physically allowed.

As the specified value of $\overline{p}_s$ is changed, the parameter space boundaries change, although the general structure remains similar. Shown in Figure 14 is the parameter space for $\overline{p}_s = 0.96395$, for which the boundary curve A is a straight line through the origin. This value has been numerically determined as follows. A sequence of solutions with decreasing B_t^* and B_p^* was evaluated, and for each pair of values $\overline{p}_s$ is adjusted until $\hat{p}(0) < 10^{-6}$ is obtained, meaning that the solution is on the boundary A. This sequence was carried out down to $B_t^* = 1.0 \times 10^{-5}$ and $B_p^* = 1.0 \times 10^{-5}$. This sub-family of solutions is referred to as S3.1, and specific solutions are further distinguished by an additional digit "n" as in S3.1n. The boundaries A and B and the points a and b have the same significance as the corresponding features in the parameter space for the sub-family S3.0 (Figure 5). For S3.1, solutions above

$B_p^* = 1.3601$ ("a") are unphysical, while those below $B_p^* = 0.7408$ ("b") are all physical.

Figures 15–21 present a number of representative solutions distributed in the allowed parameter space region, corresponding to solutions "1"–"4" shown in Figure 14, referred to as solutions S3.11–S3.14, respectively. For S3.11 ("1" in Figure 5), defined by $B_t^* = 0.14$ and $B_p^* = 0.040$, the relatively small value of B_p^* yields a small amplitude B_p component, small pinch force, and small pressure gradient, with $\mathcal{D}_p = 7.4360 \times 10^{-2}$. Note that marked difference from the Lundquist solution (dash-dot, Figure 15) or S1.1a. For S3.11, we find $\xi = 7.3379$, significantly greater than $xi_L = 1.7187$ for the Lundquist solution. Because of the small B_p component, the Alfvén speed outside the current channel is low and β is large as shown in Figure 16. For this solution, $\overline{\beta} = 2.1165 \times 10^2$.

Figure 17 shows solution S3.12 ("2"), defined by $B_t^* = 0.068$ and $B_p^* = 0.088$, which is slightly inside of boundary A. We find $\hat{p}(0) = \hat{p}_{min} \approx 0$. Note that $B_t(x)$ is much more narrowly peaked than that of S3.11, with a narrower dip in $\hat{p}(x)$. The average pressure gradient is $\mathcal{D}_p = 0.1828$. Figure 18 shows that the Alfvén speed is also narrowly peaked at $x = 0$. This solution has $\beta_{min} = 3.2383 \times 10^{-2}$ and $\overline{\beta} = 75.5251$.

Solution S3.13, shown in Figures 19 and 20, is similar to solution S3.03 (Figures 8 and 9), and its physical properties require no further discussion. This example shows that similar magnetic field profiles may correspond to different sub-classes of solutions or parameter values.

Solution S3.14 (Figures 21 and 22), indicated by the open diamond and "4" in Figure 5, is the "last" (numerically determined) physically admissible solution. This solution is specified by $B_t^* = 0.9652$ and $B_p^* = 1.3601$. It has, to within numerical uncertainty, $\hat{p}_{min} \simeq 0$ and $\beta_{min} \simeq 0$, which occurs at $x = 0.3350$ where $(V_A)_{max}/V_{A0} = 6.2481 \times 10^2$. For this solution, $\mathcal{D}_p = 1.3483$ and $\overline{\beta} = 0.3140$, with $\beta(x) \ll 1$ for $x \lesssim 1$. This solution is similar in its basic properties to S3.05.

Figure 23 shows the field and pressure profiles of solution S3.15 specified by $B_t^* = 1.0 \times 10^{-4}$ and $B_t^* = 1.0 \times 10^{-4}$. Panel (a) shows the field components (solid curves) and the magnitude of the field $|\hat{\mathbf{B}}(x)|$ (dashed). Note that $B_p \simeq 0$ so that $|\hat{\mathbf{B}}(x)| \simeq |B_t(x)|$; they are virtually indistinguishable except where $B_t(x)$ is negative. The Lundquist field components are shown (dash-dot) for comparison. Panel (b) shows the profile of the electric current $\mathbf{J}(x)$. Here, the magnitude $J(x) = |\mathbf{J}(x)|$ is shown by the dashed curve, which essentially overlaps $J_p(x)$ where it is positive ($x \lesssim 0.6$). Panel (c) shows that $\hat{p} \simeq 0$ at $x = 0$, rapidly increasing to $\hat{p} = 1$ at $x \simeq 0.4$. The average pressure gradient is $\mathcal{D}_p = 1.7958 \times 10^{-1}$. This value of $\mathcal{D}_p \ll 1$ is considerably less than the maximum pressure gradient (normalized), which is the maximum slope of $\hat{p}(x)$. This is because the bulk of the dip in pressure is localized to

$x \lesssim 0.2$. In contrast, $\mathcal{D}_p \ll 1$ is the volume-average of the pressure gradient in the entire current channel, and $d\hat{p}(x)/dx$ is weighted by x in the integrand.

The Alfvén speed (solid curve, left axis) and plasma β (dashed curve, right axis) of the system are shown in Figure 24. In this structure, $\beta \simeq 0$ near $x = 0$, but overall $\overline{\beta} = 4.4977 \times 10^6 \gg 1$, with $\beta(1) = \infty$. To within numerical accuracy, $\hat{p}(0) = 0$ and $\beta(0) = 0$. Because the temperature is assumed to be uniform throughout the system, density $n(x)$ is directly proportional to pressure $p(x)$. We find that $V_A(x)$ is essentially a spike at $x = 0$ with an infinitesimal thickness, and $\overline{\beta} \to \infty$ as the origin is approached. Thus, even though B_t^* and B_p^* both vanish, the structure remains non-force-free with $\mathcal{D}_p \neq 0$ and $\beta \to \infty$.

The properties of solutions for $\overline{p}_s > 1$ have also been examined. Shown in Figure 25 is the parameter space structure for $\overline{p}_s = 1.15$. As before, curve A is the boundary where $p(0) = 0$, and solutions acquire a nonzero imaginary curve to the right of curve B. The line segment "a" marks the upper limit beyond which no physically admissible solutions are found, while below the segment denoted by "b" all solutions are physically acceptable, as discussed earlier. Figures 26–33 provide a description of representative solutions for this sub-family of solutions, designated as "1"–"3" and "a," respectively, in Figure 25. They will be referred to as S3.21–S3.24, respectively. These solutions show no remarkable differences from those in the other sub-families discussed above. As the parameter values approach the boundary A, $\hat{p}(0)$ vanishes. However, because $\overline{p}_s > 1$, the peak in $\hat{p}(x)$ is greater, which makes the Lorentz force $J_p B_t - J_t B_p$ more negative relative to the maximum value.

Recall that for the families of solutions S1 and S2, $B_t^* \to 0$ and $B_t^* \to 0$ is the FF limit with $\mathcal{D}_p = 0$. With $\overline{p}_s \neq 1$, the pressure gradient cannot be everywhere zero so that configurations with nonzero $\overline{p}_s$ are generally not FF. For S3.0 and S3.2 discussed above, for example, the origin ($B_t^* = 0$ and $B_t^* = 0$) does not correspond to a physically allowed solution. For S3.1, the origin is on the boundary A. Thus, $\hat{p}(0) = 0$. Because $\hat{p}(1) = 1$, the flux rope necessarily has $dp(x)/dx \neq 0$ and cannot be FF.

We now consider a sub-family where the origin is in the interior of the physically allowed region. Choose $\overline{p}_s = 0.9800$. Figure 34 shows the basic parameter space structure. The solution S3.31 represented by the dot at $B_t^* = 0.02$ and $B_p^* = 0.02$, is shown in Figure 35. Note that d_5 in the definition of $b_t(x)$, equation (13), and therefore $b_t(x)$ depend on B_t^* and B_p^*. Unlike solutions in the families S1 and S2, the B_t component does not vanish because $(b_t)_{max}$ increases as $B_t^* \to 0$. The $B_p(x)$ and $Jt(x)$ components, however, are unaffected by the d_5 dependence and vanish with B_p^* as before. Here, keep in mind that $b_p(x)$ and $j_t(x)$ are independent of B_t^* and B_p^*. As a result, the need to balance the forces requires $j_p(x)$ to increase in value, which means that $b_t(x)$ must support steeper gradients, leading to a narrower dip in $\hat{p}(x)$ and a narrower peak in $b_t(x)$. Interestingly, as B_t^* and B_p^* are decreased,

the average pressure gradient increases only slowly. For S3.31, we find $\mathcal{D}_p = 9.6916 \times 10^{-2}$. The pressure profile develops a narrower and deeper dip. These solutions are not FF.

Figure 36 shows the Alfvén speed (solid, left axis) and β (dashed, right axis) for S3.31. The former is highly peaked near the axis, and $\beta(x)$ is highly nonuniform, being minimum on the axis with the value $\beta_{min} = \beta(0) = 0.8217$ but $\beta \gg 1$ throughout most of the current channel, with $\overline{\beta} = 8.8781 \times 10^2$. If a point closer to the origin is chosen, the field and current profiles remain similar except that maximum values of B_p and J_t become smaller relative to B_t and J_p, respectively, and $\overline{\beta}$ becomes much greater.

Note that the solutions shown above exhibit similar qualitative properties for all the values of $\overline{p}_s$ used here. Solutions for $\overline{p}_s = 1.20$ have also been examined and found to be similar. We have been able to find physically acceptable solutions down to $\overline{p}_s = 0.697793$; at this value "one" solution has been found, having $B_t^* = 0.4135590$ and $B_p^* = 0$. It has $p_{min} = 0$ at $x = 0.3950$. For $\overline{p}_s$ smaller than this value, we have found no physical solutions, i.e., non-negative and real $p(x)$. Note that these values are determined numerically, and there are inherent uncertainties due to numerical values. Nevertheless, the uncertainties are insignificant on the scale of the plots presented.

For the sake of completeness, the parameter space map for the family S2 is shown in Figure 37. Comparing this with Figure 2 of Paper 1, it is clear that the parameter space features are qualitatively similar with all the same physical significance.

This work was supported by the Naval Research Laboratory Base Program.

REFERENCES

Chen, J. 1996, J. Geophys. Res., **101**, 27499.

Chen, J. 2012, Astrophys. J. 2012, **761**, 179 (Paper 1).

Lundquist, S. 1950, Arkiv Fysik **2**, 361.

Shafranov, V. D. 1966, Reviews of Plasma Physics, ed. M. A. Leontovich, p. 103, Consultants Bureau, New York.

Taylor, J. B. 1974, Phys. Rev. Lett. **33**, 1139.

Woltjer, L. 1958, Proc. Nat. Acad. Sci., **44**, 489.

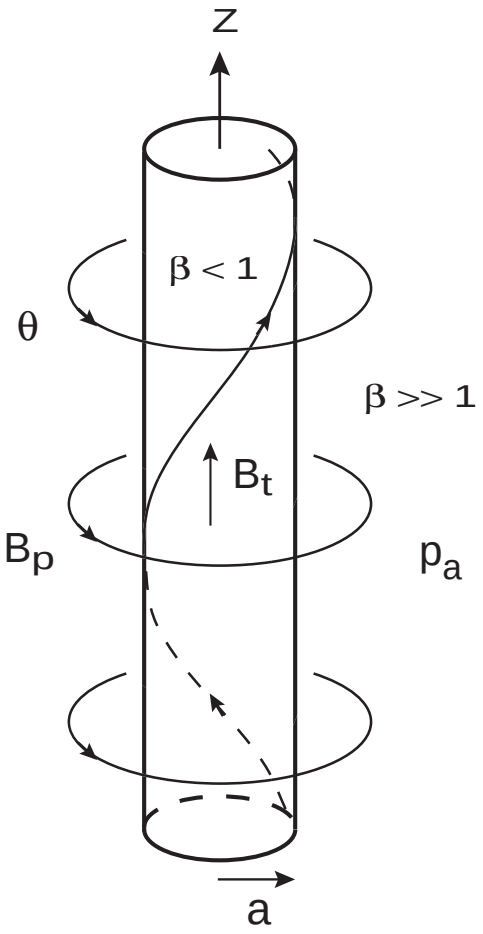

Fig. 1.— Schematic of a flux rope in equilibrium with ambient pressure p_a. The cylindrical coordinates θ and z are shown. The radial coordinate is measured from the axis at $r = 0$. The edge of the current channel is at $r = a$. Toroidal (poloidal) magnetic field component B_t (B_p) is shown. The "flux rope" consists of the current channel and the magnetic field produced by the current. The plasma β is typically much smaller inside than outside the flux rope. Reproduced from Paper 1.

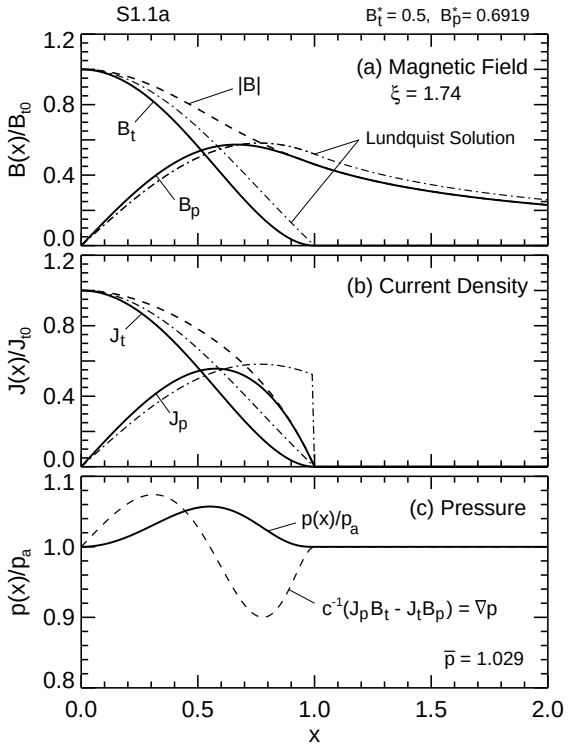

Fig. 2.— Solution S1.1a. $B_t^* = 0.50$ and $B_p^* = 0.69189841$ so that $\hat{p}(0) = 1$. (a) Magnetic field components (solid curves) and the Lundquist solution (dash-dot). Thick dashed curve is $|\mathbf{B}(x)|$. $\xi = 1.7448$. (b) Current density scaled to J_{t0}. The Lundquist current (dash-dot). Solid dashed curved is $|\mathbf{J}(x)|$. (c) Pressure $p(x)$ and dimensionless Lorentz force (dashed, arbitrary units). The average pressure gradient is $\mathcal{D}_p = 6.0637 \times 10^{-2}$ with $\hat{p}_{max} = 1.0572$.

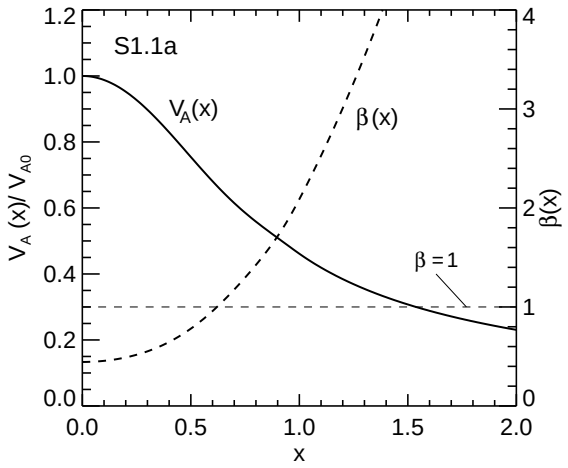

Fig. 3.— Alfvén speed $V_A(x)$ (solid curve, left axis) and $\beta(x)$ (dashed curve, right axis) for solution S1.1a. $\beta = 1$ is indicated. $\beta(0) = \beta_{min} = 0.4444$ and $\overline{\beta} = 1.2071$.

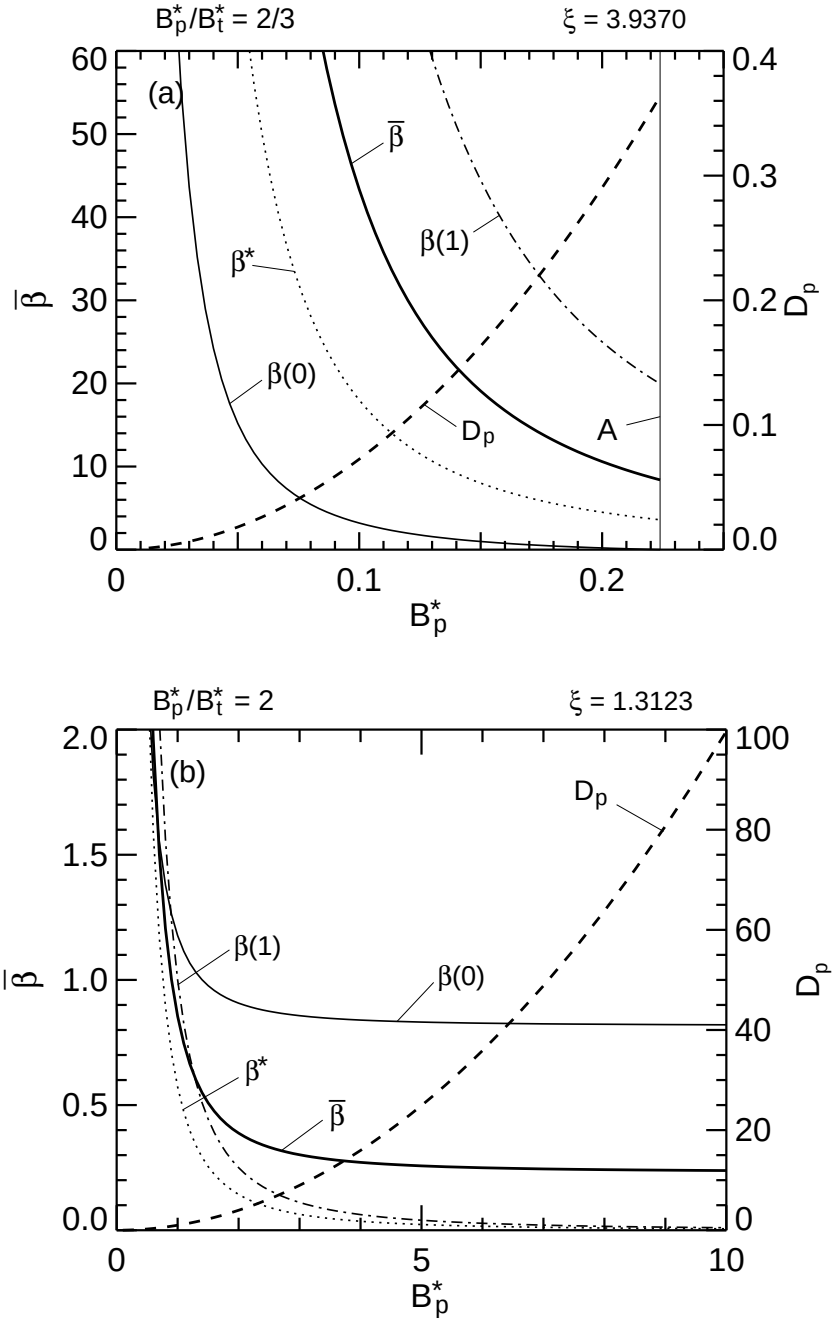

Fig. 4.— Limiting properties of $\overline{\beta}$ and $\mathcal{D}_p$ for the family of solutions S1. (a) $B_p^*/B_t^* = 2/3$. "A" indicates the intersection with curve A shown in Figure 2 of Paper 1. (b) $B_p^*/B_t^* = 2$.

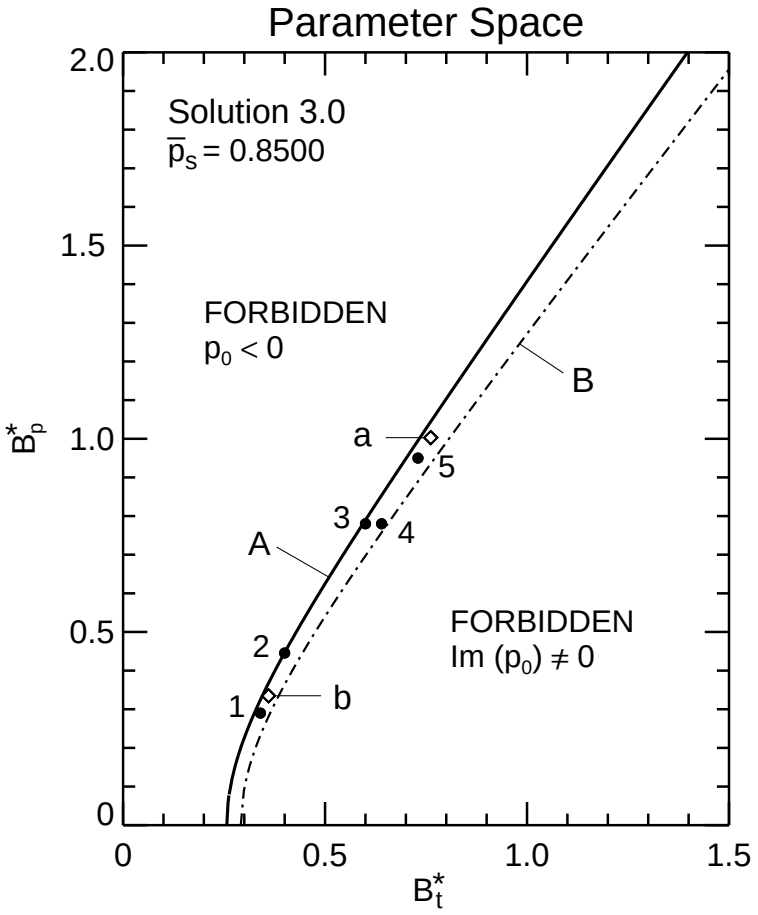

Fig. 5.— Parameter space for Particular Solution 3.0 with $\overline{p}_s = 0.85$. Solution S3.01 shown in Figure 12 of Paper 1 is marked by "1." Line segment "a" is at $B^*_p = 1.002834$, above which no physical solutions can be found, and line segment "b" is at $B^*_p = 0.3350$, below which all solutions are physical. Solutions S3.02–3.05 are indicated. The open diamond at "a" is solution S3.06 defined by $B^*_t = 0.761601$ $B^*_p = 1.002834$.

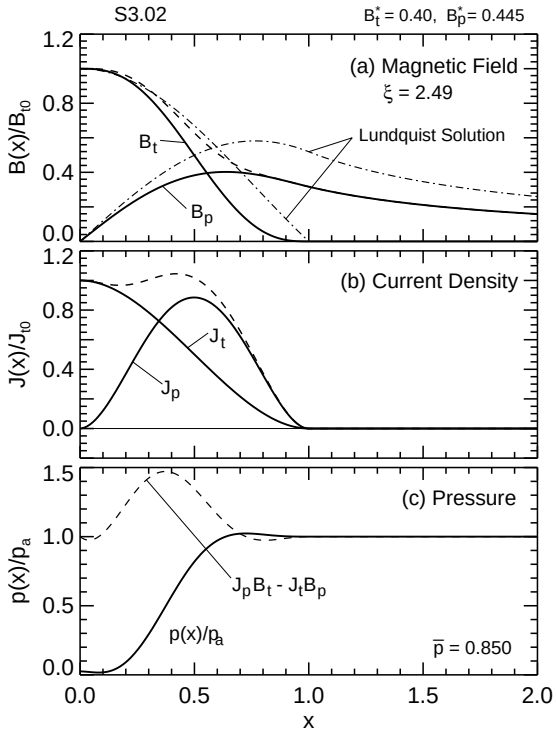

Fig. 6.— Solution S3.02 ("2" in Figure 5) given by $B_t^* = 0.40$ and $B_p^* = 0.4455$. As required, $\overline{p} = \overline{p}_s = 0.85$. $p_{min} = 1.6439 \times 10^{-2}$ at $x = 0.082$. $\mathcal{D}_p = 0.4075$. (a) Magnetic field (solid) scaled to B_{t0}, compared the Lundquist solution (dash-dot). (b) Current density scaled to J_{t0}. (c) Pressure and normalized Lorentz force (dashed). See Paper 1 for S3.01.

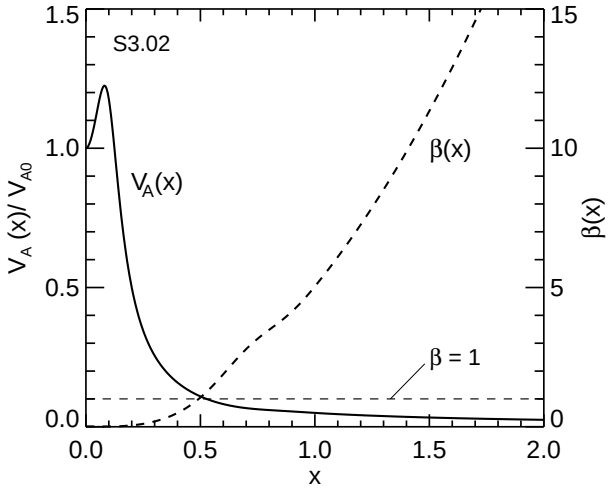

Fig. 7.— Alfvén speed $V_A(x)$ (solid curve, left axis) and $\beta(x)$ (dashed curve, right axis) for solution S3.02. $\beta = 1$ is indicated (thin dashed line). $V_A(x)$ is peaked at $x = 0.080$ where $\beta = \beta_{min} = 8.3383 \times 10^{-3}$ and and $\overline{\beta} = 2.5560$.

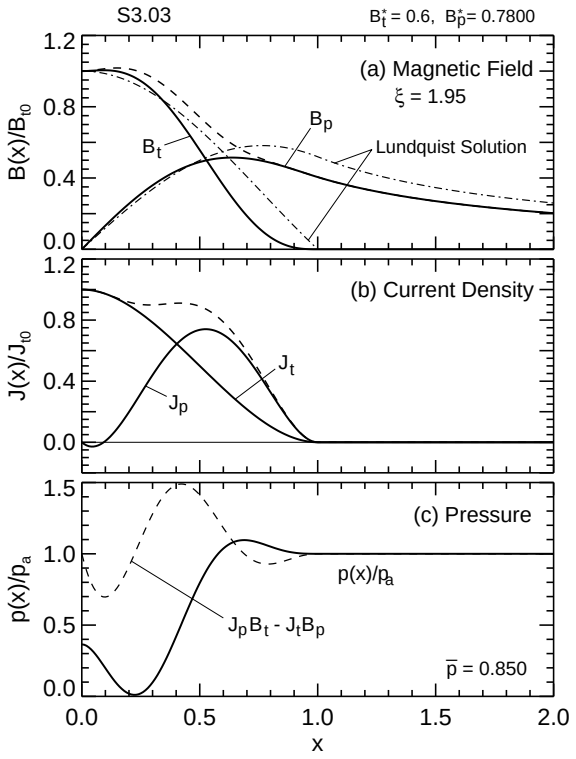

Fig. 8.— Solution S3.03 ("3") given by $B_t^* = 0.60$ and $B_p^* = 0.7800$. $J_p(x)$ is slightly negative near $x = 0$ so that $B_t(x)$ is peaked off axis. $\hat{p}_{min} = 1.0529 \times 10^{-2}$ at $x = 0.2200$ and $\hat{p}_{max} = 1.0962$ at $x = 0.6900$. $\mathcal{D}_p = 5.9044 \times 10^{-1}$.

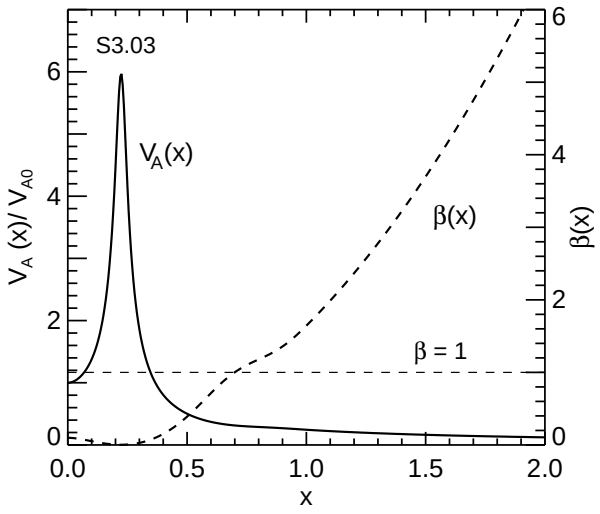

Fig. 9.— Alfvén speed $V_A(x)$ (solid, left axis) and $\beta(x)$ (dashed, right axis) for solution S3.03. $V_A(x)$ is sharply peaked at $x = 0.2200$. $\beta_{min} = 2.8046 \times 10^{-3}$ but $\overline{\beta} = 8.6924 \times 10^{-1}$.

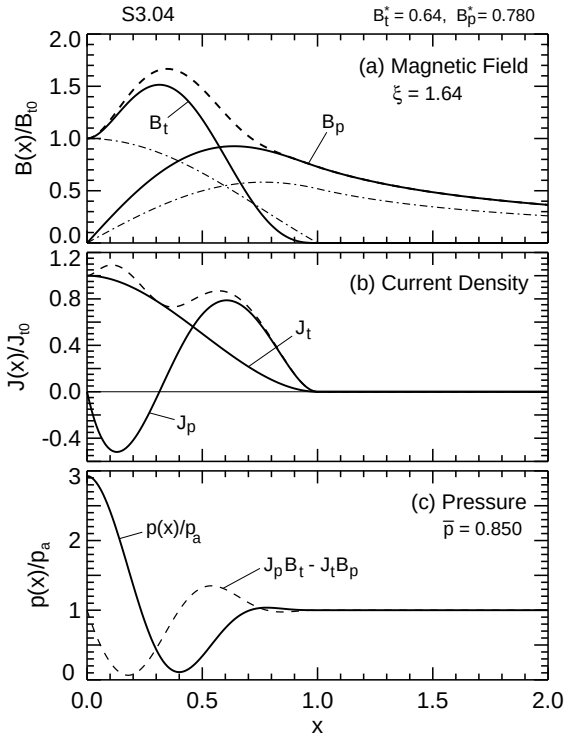

Fig. 10.— Solution S3.04 ("4") given by $B_t^* = 0.64$ and $B_p^* = 0.7800$. $J_p(x)$ is strongly negative near the axis with a significant peak in $B_t(x)$. Pressure $\hat{p}(x)$ is peaked on the axis with $\hat{p}_{max} = 2.9268$ and $\hat{p}_{min} = \hat{p}(0.4) = 1.1037 \times 10^{-1}$. $\mathcal{D}_p = 1.0801$.

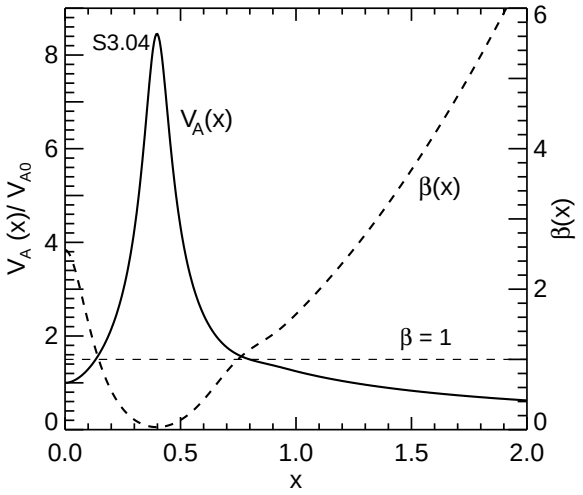

Fig. 11.— Alfvén speed $V_A(x)$ (solid, left axis) and $\beta(x)$ (dashed, right axis) for solution S3.04. $V_A(x)$ is peaked at $x = 0.40$ where $\beta(x)$ has a minimum, $\beta_{min} = 3.5829 \times 10^{-2}$. $\beta(0) = 2.5581$ and $\overline{\beta} = 8.3177 \times 10^{-1}$.

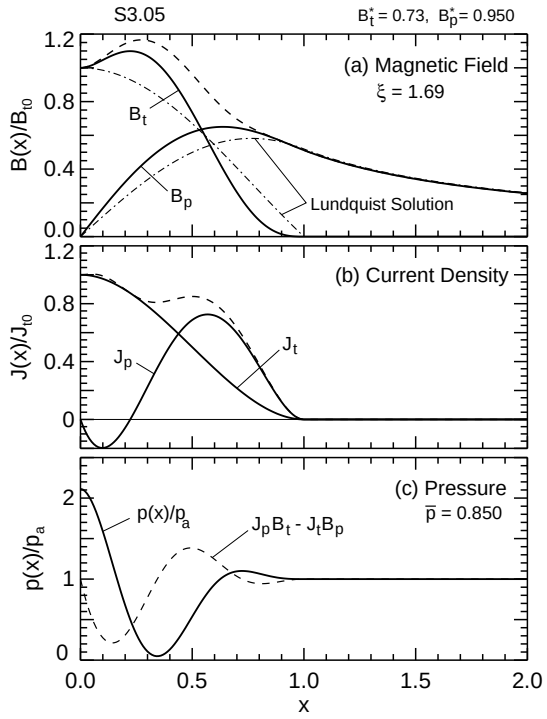

Fig. 12.— Solution S3.05 ("5") given by $B_t^* = 0.73$ and $B_p^* = 0.950$. Similar in character to S3.04. This solution has $\hat{p}_{max} = 2.1130$ and $\mathcal{D}_p = 0.9490$.

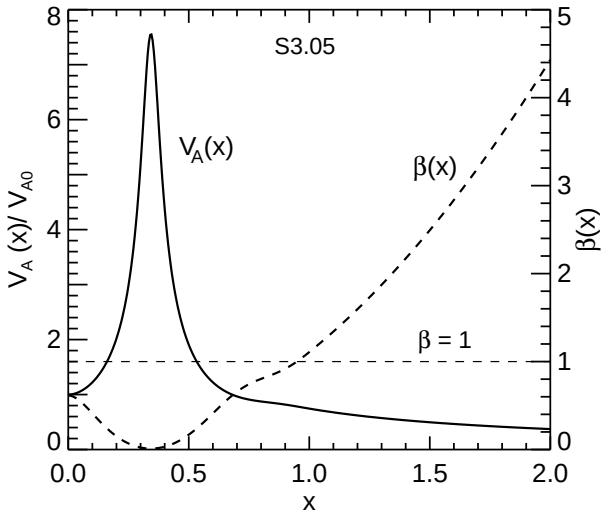

Fig. 13.— Alfvén speed $V_A(x)$ (solid, left axis) and $\beta(x)$ (dashed, right axis) for solution S3.05. $\overline{\beta} = 0.5765$ with $\beta_{min} = 1.0794 \times 10^{-2}$ at $x = 0.3400$ and $\beta(1) = 1.1080$.

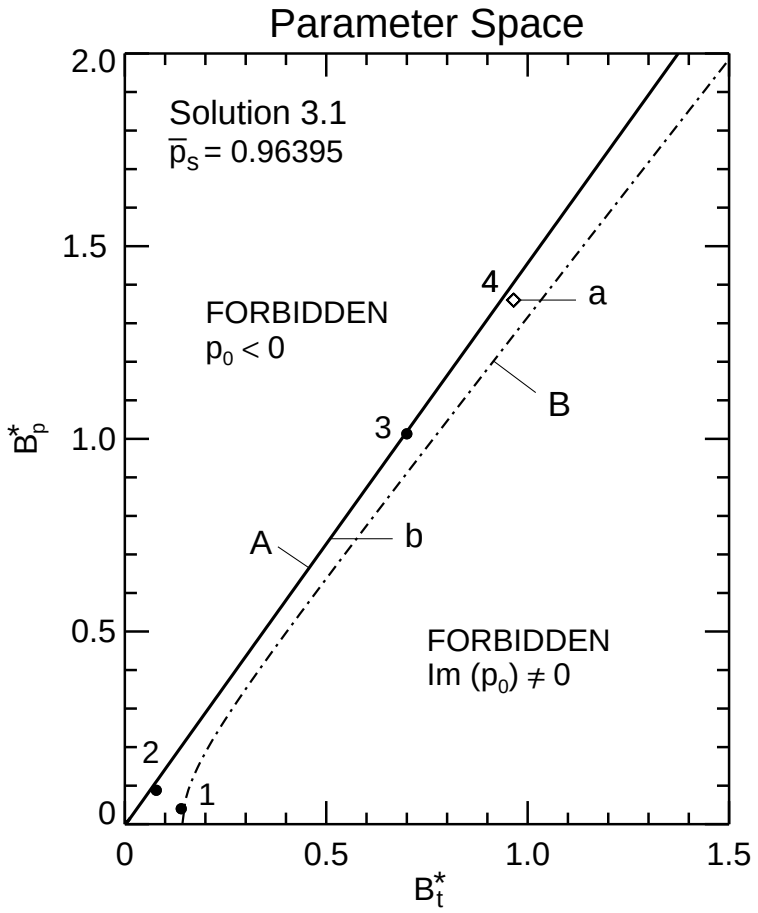

Fig. 14.— Parameter space for family S3.1 with $\overline{p}_s = 0.96395$. The equilibrium boundary A is straight and goes through the origin. Diamond "a" is at $B_t^* = 0.9652$ and $B_p^* = 1.3601$, and line "b" is at $B_p^* = 0.7408$. Above a, no physical solutions exist. Below b all solutions between A and B are physical.

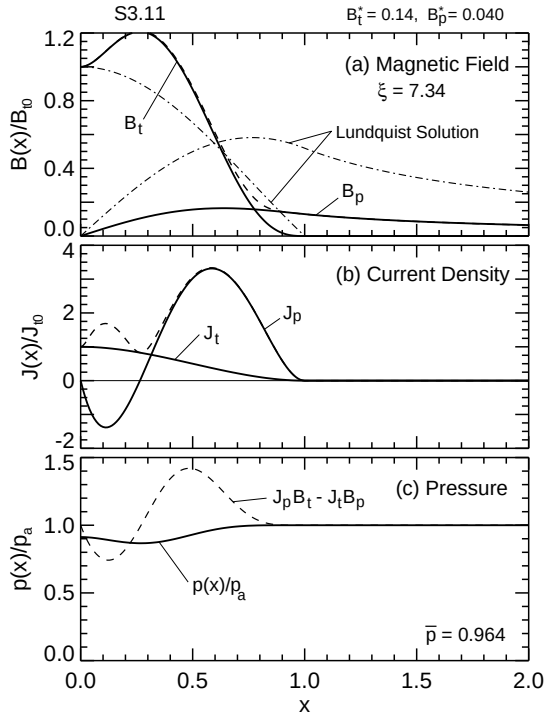

Fig. 15.— Solution S3.11 ("1" in Figure 14) with $B_t^* = 0.14$ and $B_p^* = 0.040$. Because $B_p^*/B_t^* \ll 1$, the B_t component dominates, with a peak off axis and negative J_p near the axis. $\mathcal{D}_p = 7.4360 \times 10^{-2}$. The Lundquist solution (dash-dot) is shown in panel (a).

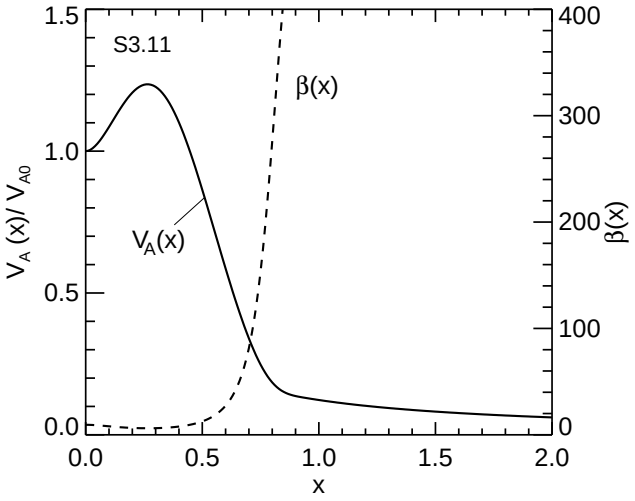

Fig. 16.— Alfvén speed $V_A(x)$ (solid, left axis) and $\beta(x)$ (dashed, right axis) for solution S3.11. $\beta \gg 1$ throughout the structure with $\beta(0) = 9.5710$, $\beta_{min} = 6.1916$, and $\overline{\beta} = 2.1165 \times 10^2$.

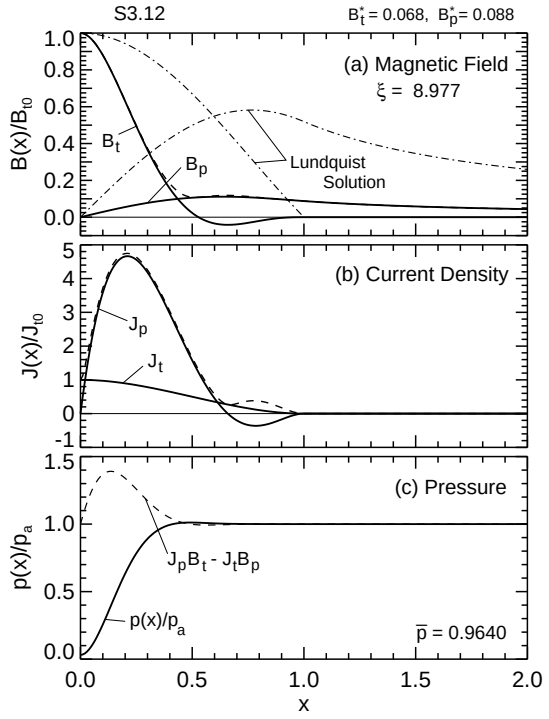

Fig. 17.— Solution S3.12 ("2") with $B_t^* = 0.068$ and $B_p^* = 0.088$. Both $B_t(x)$ and $J_p(x)$ have negative segments near $x = 1$. $\mathcal{D}_p = 0.1828$. The Lundquist field is shown in panel (a) for comparison.

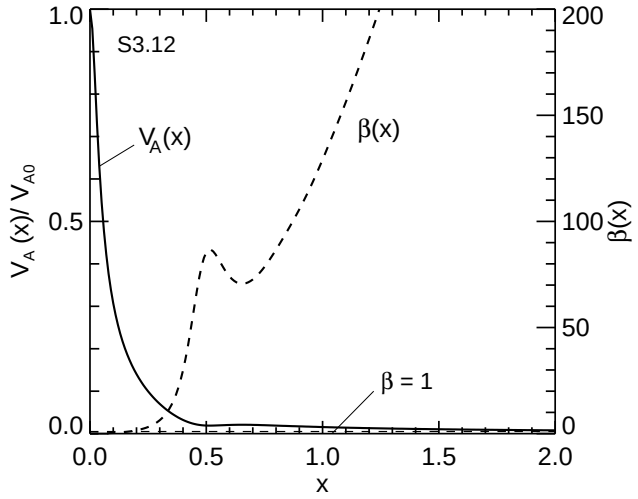

Fig. 18.— Alfvén speed $V_A(x)$ (left axis) and $\beta(x)$ (right axis) for solution S3.12. The Alfvén speed is sharply peaked on the axis, and β rapidly increases from $\beta_{min} = 3.2383 \times 10^{-2}$ at $x = 0$ and becomes much greater than unity at $x \ll 1$. $\overline{\beta} = 75.5251$.

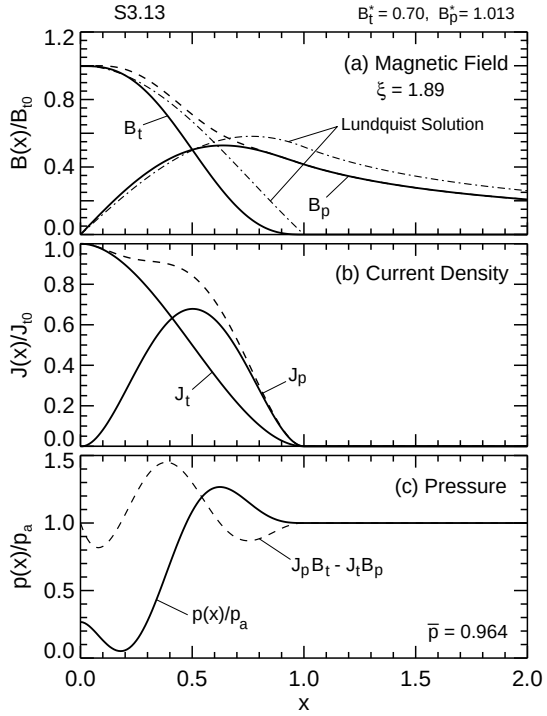

Fig. 19.— Solution S3.13 ("3") defined by $B_t^* = 0.70$ and $B_p^* = 1.013$. $\hat{p}_{max} = 1.2666$ at $x = 0.6200$, $\hat{p}_{min} = 5.2032 \times 10^{-2}$ at $x = 0.1800$, and $\mathcal{D}_p = 0.7023$. The field profiles are similar to those of the Lundquist solution (dash-dot curves).

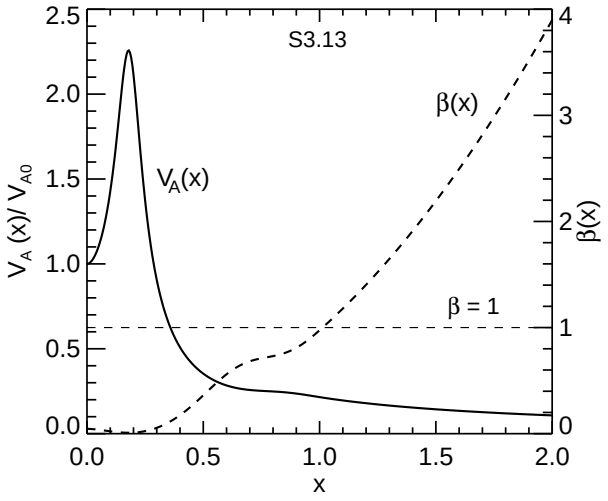

Fig. 20.— Alfvén speed $V_A(x)$ (left axis) and $\beta(x)$ (right axis) for solution S3.13. $(V_A)_{max}/V_{A0} = 2.2569$. $\beta \ll 1$ for $x \lesssim 0.3$ with $\beta(0) = 4.5160 \times 10^{-2}$ and $\overline{\beta} = 5.7220 \times 10^{-1}$.

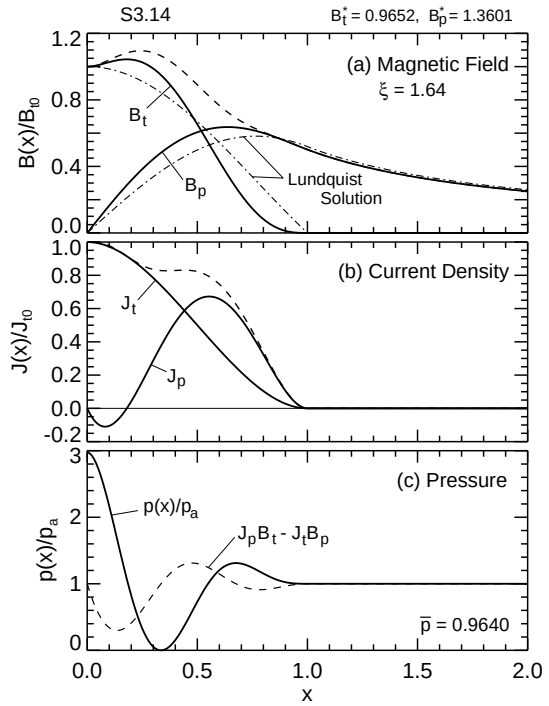

Fig. 21.— Solution S3.14 ("4") given by $B_t^* = 0.9652$ and $B_p^* = 1.3601$, denoted by the open diamond "a" in Figure 14. The only physical solution at $B_p^* = 1.3601$. $J_p(x)$ is negative slightly off the axis. $\mathcal{D}_p = 1.3483$.

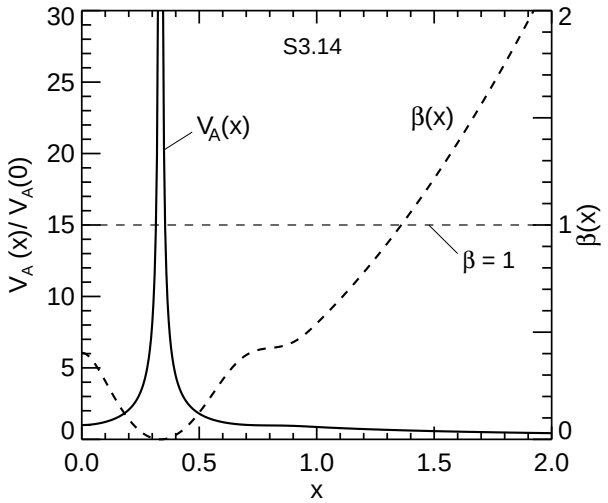

Fig. 22.— Alfvén speed $V_A(x)$ (solid curve, left axis) and $\beta(x)$ (dashed curve, right axis) for solution S3.14. $(V_A)_{max}/V_{A0} = 1.4134 \times 10^2$. The flux rope has $\overline{\beta} = 3.1395 \times 10^{-1}$ with $\beta_{min} = 2.0231 \times 10^{-5}$ at $x = 0.34$. For this flux rope, $\beta \ll 1$ for all $x \leq 1$.

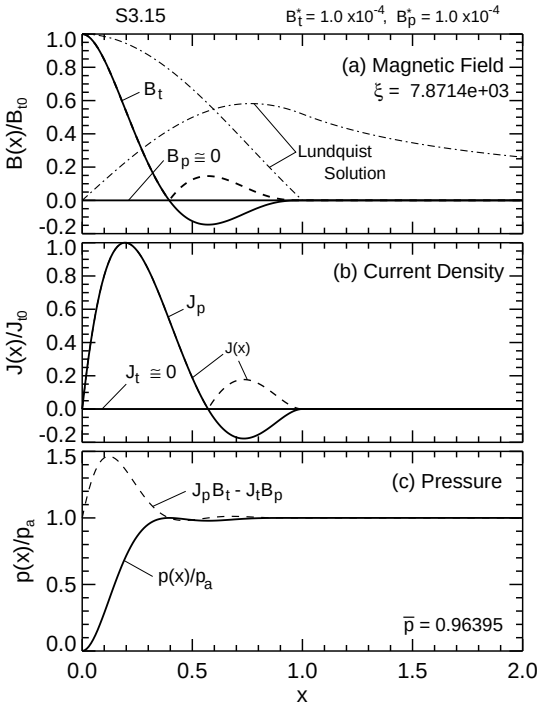

Fig. 23.— Solution S3.15 given by $B_t^* = 10^{-4}$ and $B_p^* = 10^{-4}$. The average pressure gradient is $\mathcal{D}_p = 1.7958 \times 10^{-1}$. To within the numerical accuracy, $V_A(0) \simeq \infty$ because $\hat{p}(0) \simeq 0$.

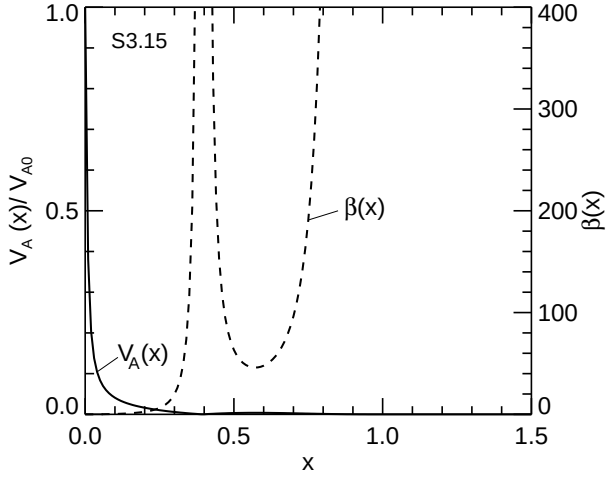

Fig. 24.— Alfvén speed $V_A(x)$ (solid curve, left axis) and $\beta(x)$ (dashed curve, right axis) for solution S3.15. $V_A(x)$ is essentially a spike at $x = 0$, decreasing from $V_A/V_{A0} = 1$ to $V_A/V_{A0} = 0.1$ at $x \simeq 0.04$ and to $V_A/V_{A0} = 0.01$ at $x \approx 0.25$. $\beta(0) = 6.6474 \times 10^{-4}$ but overall $\overline{\beta} = 4.4977 \times 10^6 \gg 1$.

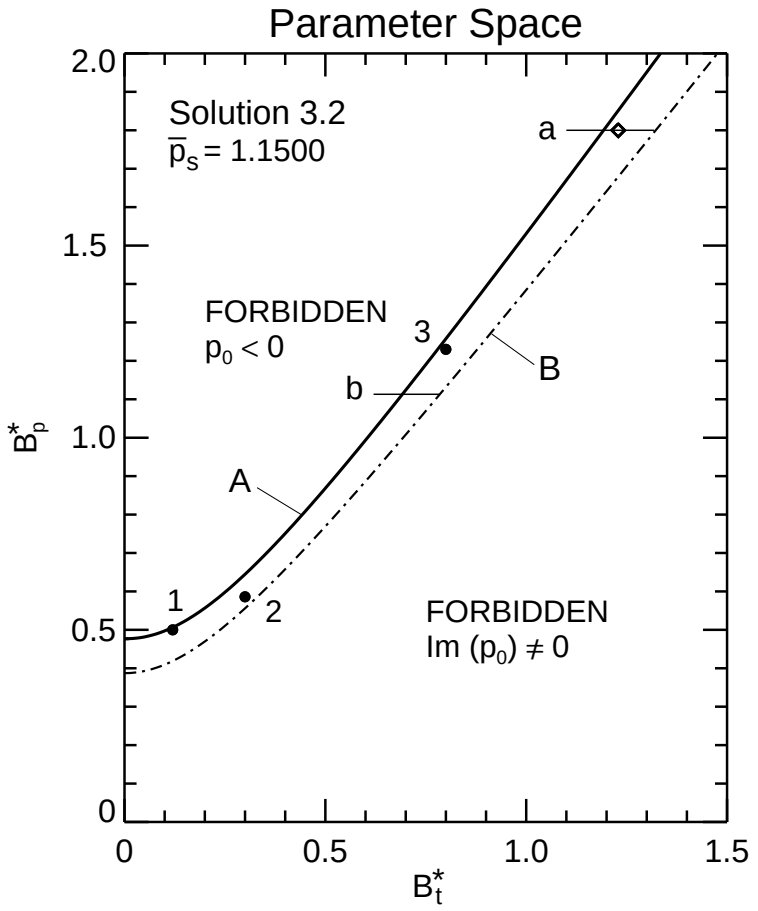

Fig. 25.— Parameter space for family S3.2 with $\overline{p}_s = 1.1500$. Line segment "a" is at $B_p^* = 1.80004$ and "b" is at $B_p^* = 1.11306$. At a, one physical solution (open diamond) exist, and above "a" no physical solutions exist. Below b all solutions between A and B are physical. To the left of A, $\hat{p}(0) < 0$, and to the right of B, $\hat{p}(x)$ has a nonzero imaginary part.

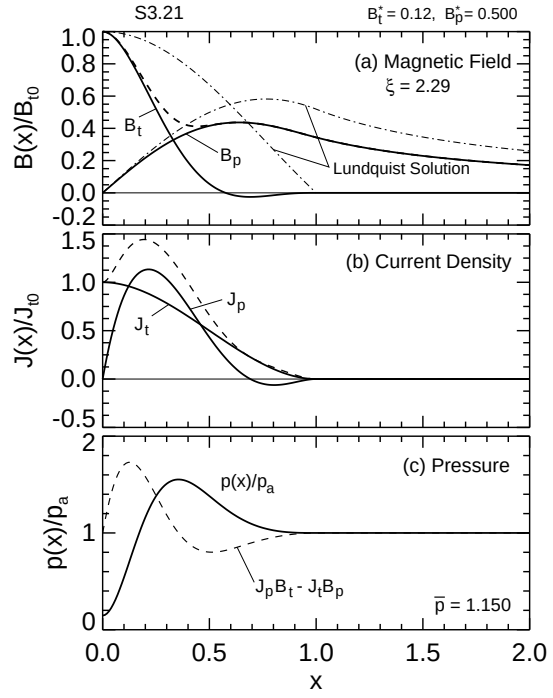

Fig. 26.— Solution S3.21 ("1" in Figure 25) given by $B_t^* = 0.12$ and $B_p^* = 0.50$. $J_p(x)$ has a negative segment near $x = 1$. $\hat{p}_{min} = 0.1466$ and $\hat{p}_{max} = 1.5527$ at $x = 0.36$. $\mathcal{D}_p = 0.5331$.

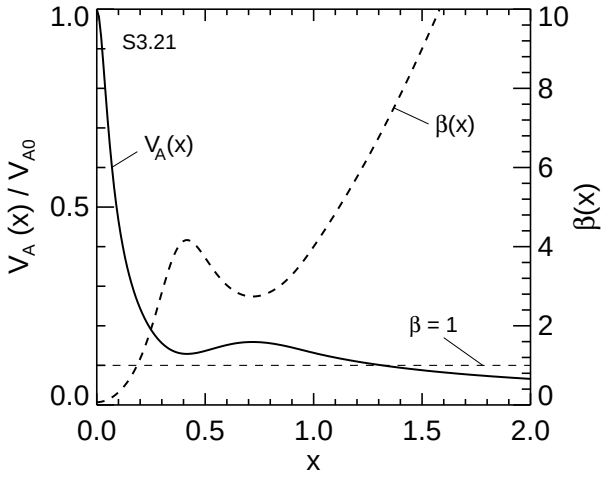

Fig. 27.— Alfvén speed $V_A(x)$ (left axis) and $\beta(x)$ (right axis) for solution S3.21. $V_A(x)$ is sharply peaked at $x = 0$. Except near the axis, $\beta \gg 1$ with $\overline{\beta} = 3.1029$.

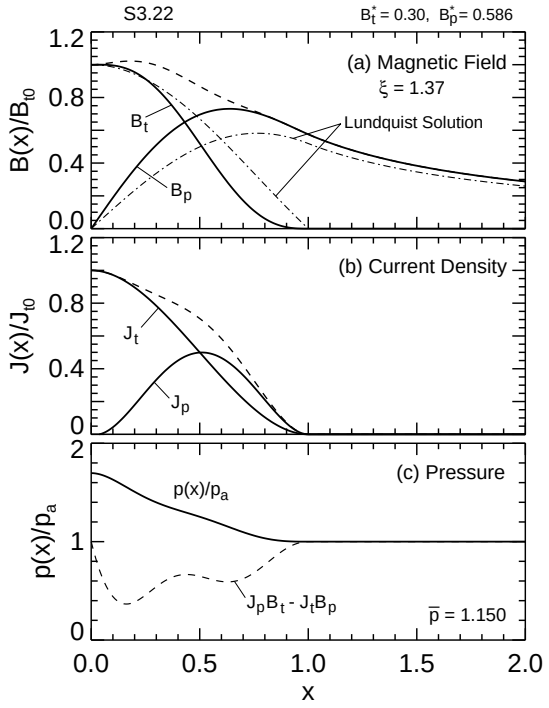

Fig. 28.— Solution S3.22 ("2") given by $B_t^* = 0.30$ and $B_p^* = 0.586$. $\mathcal{D}_p = 0.2771$.

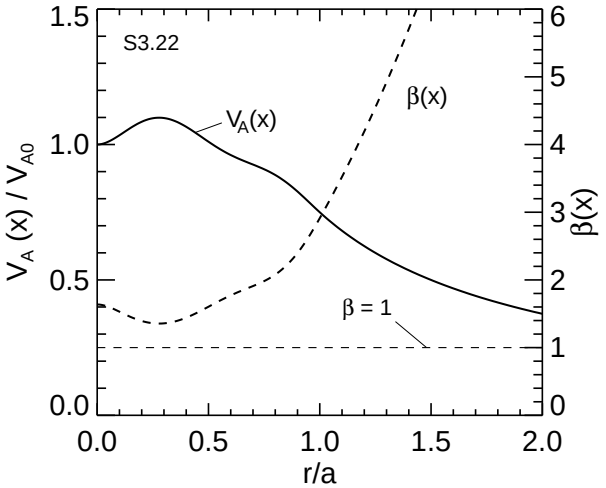

Fig. 29.— Alfvén speed $V_A(x)$ (left axis) and $\beta(x)$ (right axis) for solution S3.22. $V_A(x)$ has a broad and gentle peaked. $\beta > 1$ throughout the flux rope, having $\overline{\beta} = 1.9670$.

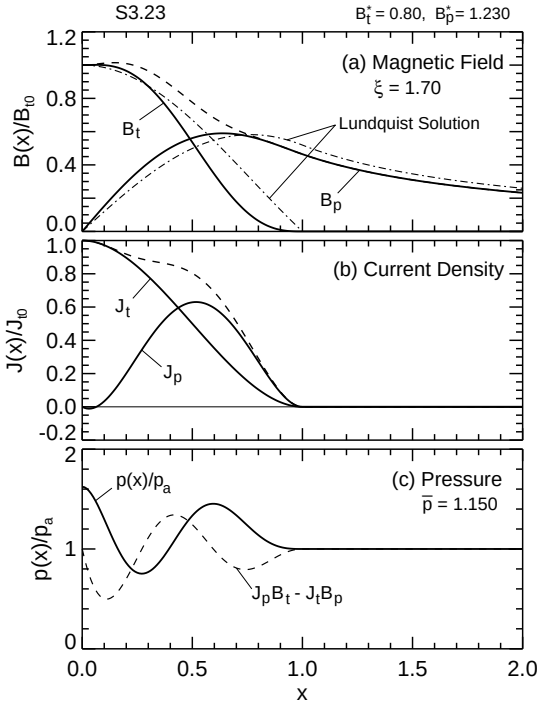

Fig. 30.— Solution S3.23 ("3") given by $B_t^* = 0.80$ and $B_p^* = 1.230$. $\mathcal{D}_p = 0.7509$.

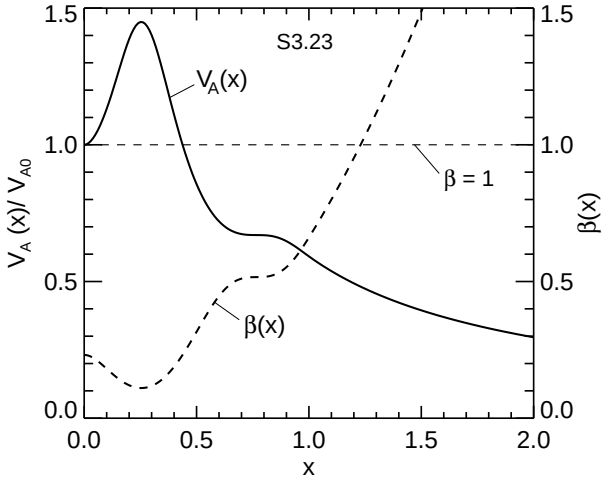

Fig. 31.— Alfvén speed $V_A(x)$ (left axis) and $\beta(x)$ (right axis) for solution S3.23. $\beta < 1$ throughout the current channel with $\overline{\beta} = 0.4325$.

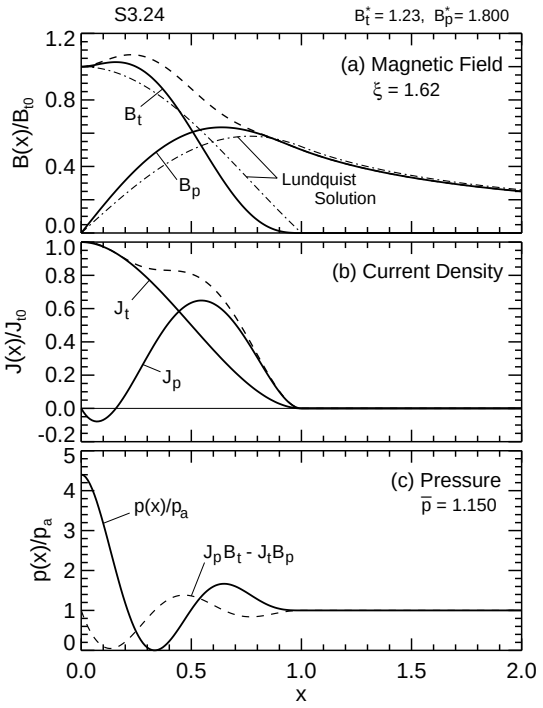

Fig. 32.— Solution shown by an open diamond at "a" at $B_t^* = 1.22824$ and $B_p^* = 1.79972$, the only physical solution at this value of B_p^*. $\hat{p}_{min} = 0$ at $x = 0.33$. $\mathcal{D}_p = 1.9912$.

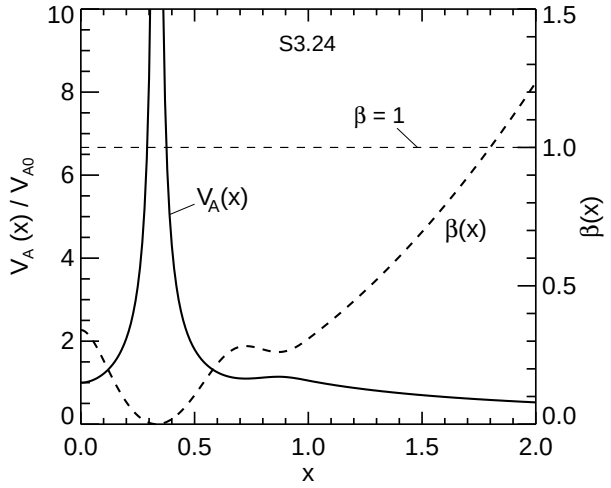

Fig. 33.— $V_A(x)$ (solid, left axis) and $\beta(x)$ (dashed, right axis) for solution "a". $(V_A)_{max}/V_{A0} = 1.6869 \times 10^3$, $\beta_{min} = 0$ at $x = 0.33$, $\overline{\beta} = 0.2060$, and $\beta(x) \ll 1$ for all $x \leq 1$.

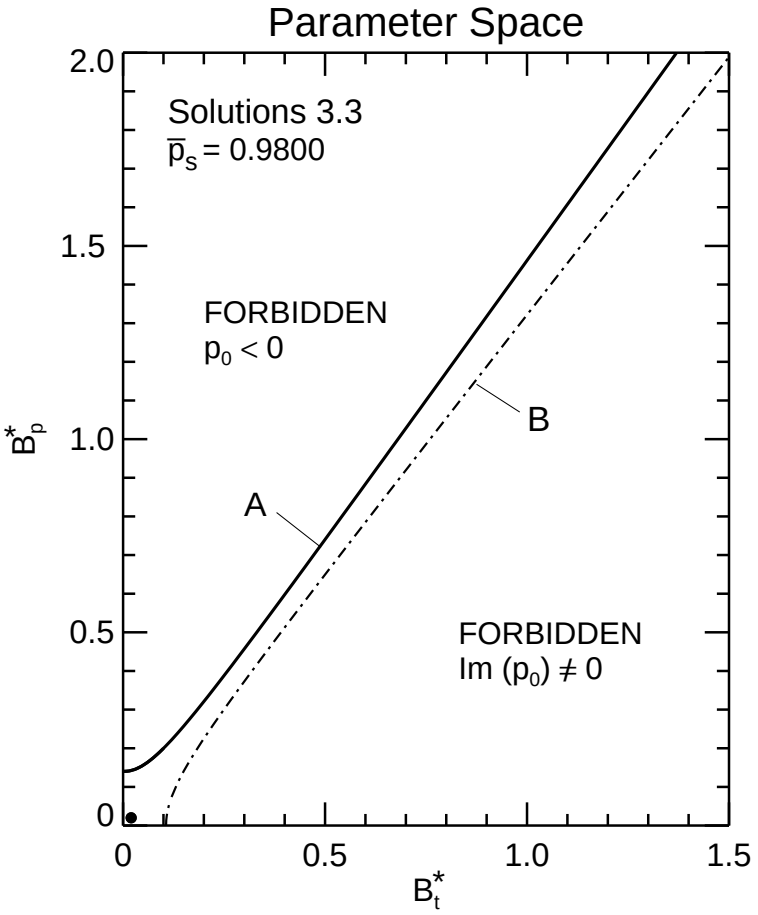

Fig. 34.— Parameter space for family S3.3 with $\overline{p}_s = 0.9800$. The origin, $B_t^* = 0$ and $B_p^* = 0$, is in the physically allowed region.

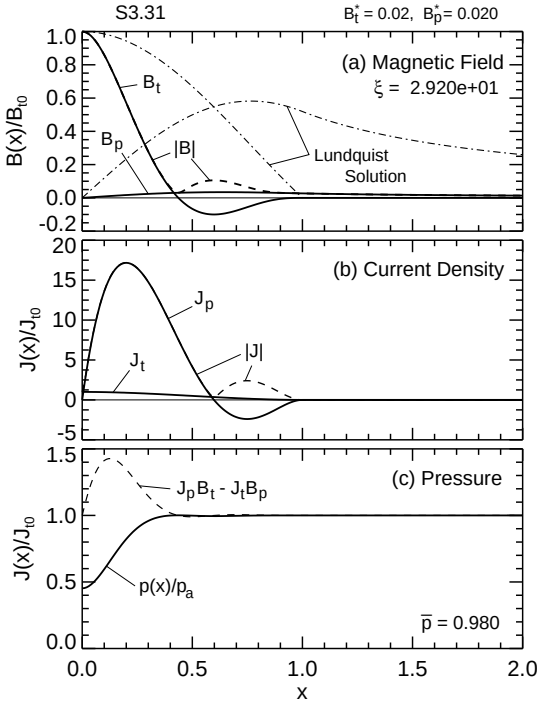

Fig. 35.— Solution S3.31 given by $B_t^* = 0.02$ and $B_p^* = 0.02$ and indicated by the dot in Figure 34. $\mathcal{D}_p = 9.6916 \times 10^{-2}$.

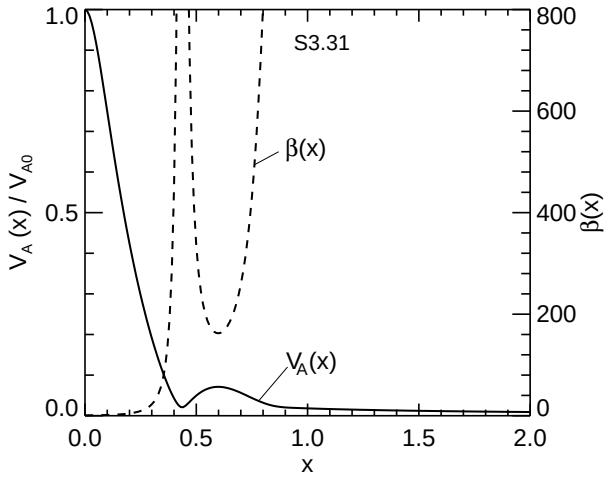

Fig. 36.— $V_A(x)$ (left axis, solid curve) and $\beta(x)$ (right axis, dashed curve) for solution "a". $\beta_{min} = \beta(0) = 0.8217$ at $x = 0$, but $\overline{\beta} \approx 8.8781 \times 10^2 \gg 1$.

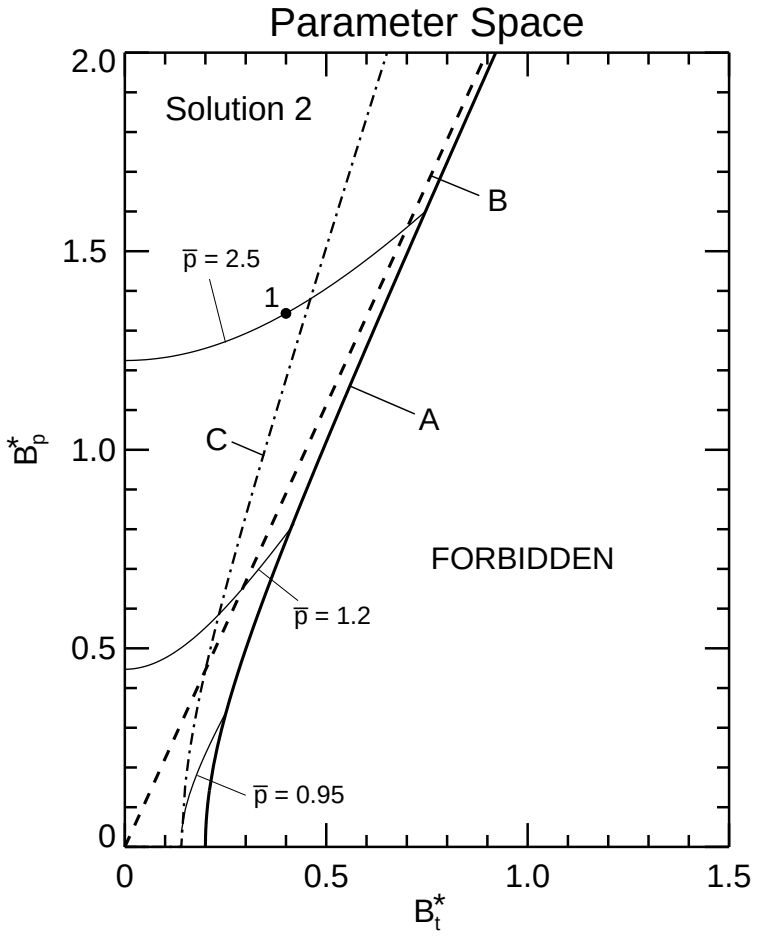

Fig. 37.— Parameter space for Particular Solution 2 to be compared with that for Solution 1 shown in Paper 1, where solution S2.1 indicated by point "1" is discussed.